

A human-like model of aniridia-associated keratopathy for mechanistic and therapeutic studies

Dina Javidjam, ... , Yedizza Rautavaara, Neil Lagali

JCI Insight. 2024. <https://doi.org/10.1172/jci.insight.183965>.

Research In-Press Preview Ophthalmology Stem cells

Aniridia is a rare congenital condition of abnormal eye development arising principally from heterozygous mutation of the *PAX6* gene. Among the multiple complications arising in the eye, aniridia-associated keratopathy (AAK) is a severe vision-impairing condition of the cornea associated with a progressive limbal stem cell deficiency that lacks suitable treatment options. Current mouse models of aniridia do not accurately represent the onset and progression dynamics of human AAK, hindering therapy development. Here, we performed deep phenotyping of a haploinsufficient *Pax6*^{+/-} small-eye (Sey) mouse model on the 129Sey/SvImJ background, that exhibits key features of mild presentation at birth and progressive AAK with aging, mimicking human disease. The model exhibits a slowly progressing AAK phenotype and provides new insights into the disease including disturbed basal epithelial cell organization, function and marker expression, persistent postnatal lymphangiogenesis, disrupted corneal innervation patterns, and persisting yet altered limbal stem cell marker expression with age. The model recapitulates many of the known features of human disease, enabling investigation of underlying disease mechanisms and importantly, to access a well-defined temporal window for evaluating future therapeutics.

Find the latest version:

<https://jci.me/183965/pdf>



1 **A human-like model of aniridia-associated keratopathy for mechanistic and**
2 **therapeutic studies**

3 Dina Javidjam, Petros Moustardas, Mojdeh Abbasi, Ava Dashti, Yedizza Rautavaara, Neil
4 Lagali*

5

6 Division of Ophthalmology, Department of Biomedical and Clinical Sciences, Linköping
7 University, Linköping, Sweden

8

9 *Corresponding author: Neil Lagali, SE-581 83 Linköping, Sweden, neil.lagali@liu.se,

10 Tel. +46 700 850953

11

12 ORCID:

13 Dina Javidjam: 0000-0003-4436-5928

14 Petros Moustardas: 0000-0003-3192-3708

15 Mojdeh Abbasi: 0000-0002-3641-0621

16 Ava Dashti: 0000-0001-6809-8348

17 Yedizza Rautavaara: 0009-0008-5508-5554

18 Neil Lagali: 0000-0003-1079-4361

19

20 Conflict-of-Interest Statement:

21

22 The authors have declared that no conflict of interest exists.

23 **Abstract**

24 Aniridia is a rare congenital condition of abnormal eye development arising principally from
25 heterozygous mutation of the *PAX6* gene. Among the multiple complications arising in the
26 eye, aniridia-associated keratopathy (AAK) is a severe vision-impairing condition of the
27 cornea associated with a progressive limbal stem cell deficiency that lacks suitable treatment
28 options. Current mouse models of aniridia do not accurately represent the onset and
29 progression dynamics of human AAK, hindering therapy development. Here, we performed
30 deep phenotyping of a haploinsufficient *Pax6*^{+/-} small-eye (Sey) mouse model on
31 the 129Sey/SvImJ background, that exhibits key features of mild presentation at birth and
32 progressive AAK with aging, mimicking human disease. The model exhibits a slowly
33 progressing AAK phenotype and provides new insights into the disease including disturbed
34 basal epithelial cell organization, function and marker expression, persistent postnatal
35 lymphangiogenesis, disrupted corneal innervation patterns, and persisting yet altered limbal
36 stem cell marker expression with age. The model recapitulates many of the known features of
37 human disease, enabling investigation of underlying disease mechanisms and importantly, to
38 access a well-defined temporal window for evaluating future therapeutics.

39

40 **Keywords:** congenital aniridia, aniridia-associated keratopathy, Sey mouse model, Limbal
41 stem cell deficiency, angiogenesis, lymphangiogenesis

42 **Introduction**

43 Congenital aniridia is a disorder of disrupted normal eye development owing to
44 haploinsufficiency of the PAX6 protein caused by heterozygous mutations of the *PAX6* gene
45 (1). Underdeveloped eye structures lead to multiple ocular pathologies including iris and
46 foveal hypoplasia. Additionally early-onset glaucoma, and cataracts are reported, that may
47 arguably be attributed to abnormal trabecular meshwork differentiation (1,2), Importantly, in
48 most cases the development of aniridia-associated keratopathy (AAK) becomes the vision-
49 limiting factor. AAK is a slow-onset, progressive loss of corneal transparency associated with
50 inflammation, neovascularization, and an insufficiency of limbal stem cells that normally
51 constantly renew the corneal epithelium. The prevalence and severity of AAK tends to
52 increase as patients age, with progressive limbal stem cell deficiency, pervasive inflammation
53 and neurodegeneration present in the cornea, and with surgical interventions unfortunately
54 proving ineffective (3,4), leading to blindness with poor prognosis for subsequent
55 interventions (5). To develop more effective and targeted therapies, a deeper understanding of
56 the mechanisms leading to AAK and its progression is needed - thus, a relevant and accurate
57 model of AAK is essential.

58 Mice are an excellent model for congenital aniridia as the human *PAX6* and mouse *Pax6*
59 genes are identical and encode the same amino acid sequence. Transgenic mice with an
60 aniridia phenotype are created by targeted mutation of one allele of the *Pax6* gene (called the
61 Sey allele, for 'small-eye') resulting in mutant mice exhibiting a spectrum of AAK
62 phenotypes. As about 70% of all human cases of aniridia result from premature termination
63 codon (PTC) mutations leading to nonsense-mediated PAX6 protein decay (6,7), this
64 mutation type is the most useful for investigating disease mechanisms. Potential therapeutics
65 also exist for this type of mutation, such as nonsense-suppression drugs (also called read-
66 through drugs) designed to ignore the PTC and thereby produce a full-length PAX6 protein

67 that does not degrade (8,9). Likewise, the genetic background is a significant factor affecting
68 the ocular phenotype. The Sey allele on the C57BL/6 genetic background results in significant
69 variability, with moderate to severe microphthalmia and structural abnormalities; however,
70 microphthalmia is seldom reported in aniridia. Moreover, mutations on C57BL/6 and Balb/c
71 backgrounds result in an aggressive, advanced AAK phenotype apparent upon eye opening in
72 the early postnatal period (6,10,11). This is a clear departure from the majority of human
73 aniridia cases, where the cornea is transparent and presents with a very mild AAK that
74 generally does not progress during the first decade of life (12). Consequently, a critical
75 therapeutic window for aniridia that exists early in life in humans (1,12) has been inaccessible
76 for therapy development in mouse models.

77 The *Pax6*^{+/-} haploinsufficient small eye (Sey) mouse model on the 129S1/SvImJ and hybrid
78 F1 backgrounds was recently presented as an alternative aniridia model (11) that has a PTC
79 mutation representing the most frequent human aniridia-causing mutation type. In particular,
80 the mouse model on the 129S1/SvImJ background exhibited slower development of corneal
81 neovascularization, but the full characteristics of the model on this background, including the
82 ocular and AAK phenotype, are largely unknown. Here, we perform deep phenotype
83 characterization of the dynamics of AAK development in this model, to evaluate its
84 relationship to human disease. We provide a comprehensive analysis of the histologic,
85 morphometric, and immunohistochemical features of the cornea in this mouse model with
86 heterozygous *Pax6*^{+/-} genotype, relative to wild-type (*Pax6*^{+/+}) littermates, showing that the
87 model mimics the human disease and provides a previously inaccessible potential therapeutic
88 window for AAK, to facilitate detailed mechanistic and therapeutic investigations of
89 relevance for human congenital aniridia.

90 **Results**

91 ***Pax6*^{+/-} haploinsufficient 129S1/SvImJ heterozygous (Het) mice exhibit human-like** 92 **delayed onset AAK phenotypes.**

93 The Het phenotype was visually discernible in adult mice upon observation, with smaller eye
94 openings and more closed eyelids (Figure 1A). Relative to wild-type (Wt) mice on the same
95 background, hematoxylin and eosin (H&E) staining revealed defects in Het mice such as
96 keratolenticular adhesion, shallow anterior chamber, thickened cornea at the site of
97 attachment, and iridocorneal angle abnormalities (Figure 1B). Examining the level of PAX6
98 protein, Western blot (Figure 1C) showed a PAX6 protein level of 42% in Het mice relative
99 to Wt ($P < 0.001$).

100 To assess AAK development, 26 Het mice and 24 Wt mice were characterized longitudinally,
101 with monthly examination up to five months using slit lamp biomicroscopy. In Wt mice, a
102 fully transparent cornea with full iris remained unchanged up to 5 months (Figure 1D, Figure
103 1E, top row). In Het mice, the onset of AAK was variable and progressive, as assessed by the
104 degree of central corneal opacity (loss of transparency). Central corneal opacity progressively
105 increased with age in Het mice while Wt corneas remained transparent (Figure 1D). In eyes
106 exhibiting AAK (defined by the degree of blood vessel invasion into the cornea), two general
107 phenotypes were apparent. In the ‘early AAK’ phenotype, invasion of blood vessels into the
108 cornea occurred first at 1-2 months of age, gradually progressing from the periphery to the
109 center of the cornea at 5 months of age (Figure 1E, middle row). In the second ‘late AAK’
110 phenotype, vessel invasion was apparent first at 4-5 months of age (Figure 1E, bottom row).

111 **Abnormalities in the cornea, lens, and iris in Het mice**

112 Table 1 provides a summary of the various abnormalities observed in the eyes of up to 60 Het
113 mice by in vivo slit lamp and in vivo confocal microscopy (IVCM) examinations in mice of
114 different ages. There was no significant sex differences noted in any of the parameters at the

115 different ages (Supplementary Table S1). The diverse frequencies of abnormal findings in
116 Table 1 reflect the varied phenotypes induced by AAK. However, keratolenticular (cornea-
117 lens) adhesion was the most consistent feature observed in 100% of eyes in Het mice by
118 IVCM examination, a feature observed even at a late prenatal stage (Supplementary Figure
119 S4). The adhesion appeared in vivo as a dark ring structure in the posterior stroma (Figure
120 2A). In 15-20 % of eyes of Het mice, dark vacuole structures were visible in the posterior
121 stroma near the keratolenticular adhesion (Figure 2B). Occasionally, this adhesion was
122 minimal and challenging to detect with a slit lamp. However, further IVCM investigation
123 confirmed the presence of adhesion (Supplementary Figure S1). Adhesions could also be
124 confirmed by optical coherence tomography (OCT) examination, scanning the cornea in all
125 directions. Infiltration of inflammatory cells into the corneal stroma was observed in up to
126 33% of eyes of Het mice at various ages (Figure 2C). The second most common feature
127 observed in the cornea was neuromas, observed by IVCM imaging as a group of prominent
128 nerve endings present at the termination point of a stromal nerve trunk (Figure 2D).

129 Iris coloboma was present in about half of corneas from Het mice at all ages, with variable
130 degree and patterns of coloboma apparent (Supplementary Figure S2). The persistence of lens
131 remnants within the cornea is depicted in histology and in vivo by OCT in the same eyes in
132 Figure 2E. Separation of the lens vesicle from the surface ectoderm during fetal development
133 was incomplete in Het mice, resulting in keratolenticular adhesions of various degrees.

134 **Het mice exhibit thinner corneas and a compromised epithelial barrier**

135 OCT images revealed a fully developed anterior chamber with clear and consistent
136 iridocorneal angle in Wt mice, but markedly shallower anterior chamber depth in the eyes of
137 Het mice, which was about half the depth of Wt ($P < 0.0001$, Figure 3A,B). Central corneal
138 thickness was measured from OCT images of 235 eyes, with corneas of Het mice being

139 28.7% thinner than Wt mice at 1 month of age ($P < 0.0001$), retaining this reduction up to 5
140 months (Figure 3C).

141 Histological investigation of the cornea revealed loss of columnar structure of basal epithelial
142 cells, resulting in flattening of basal epithelial cells and loss of the distinctive contrast pattern
143 of nuclear staining in corneas of Het mice relative to Wt mice (Figure 3D). The corneal
144 epithelium in Het mice also appeared markedly thinner than the Wt corneal epithelium
145 (Figure 3D). As basal cells build the epithelial basement membrane by producing and
146 secreting components such as collagen IV (COL4), this was also examined. A distinct loss of
147 collagen IV expression in the cornea of Het mice was noted and an epithelial basement
148 membrane was not discernible. Additionally, loss of collagen IV expression within the
149 cytoplasm of basal epithelial cells was noted (Figure 3E). A dot-like expression pattern of
150 collagen IV was apparent in the corneal stroma of Wt mice, representing basement membrane
151 surrounding corneal nerves (13), which was also visible in corneas of Het mice to some extent
152 (Figure 3E). Staining of the live cornea with fluorescein dye and imaging under blue light
153 confirmed impairment of the epithelial barrier function, with stromal uptake of the dye visible
154 in corneas of Het mice (Figure 3F).

155 Quantitative analysis of H&E stained sections confirmed that relative to the Wt mice, the
156 corneal epithelium in corneas of Het mice was half the thickness ($P < 0.0001$, Figure 3G).
157 Additionally, the mean number of stratified cell layers in the epithelium was reduced from 5
158 in Wt to 3 in Het mice ($P < 0.0001$, Figure 3H). Basal epithelial cell layer thickness was
159 likewise reduced in Het mice ($P < 0.0001$, Figure 3I). Basal epithelial cell density in Het mice
160 was also reduced, with a significant reduction in the number of basal cells per 100 μm of
161 linear distance ($P < 0.0001$, Figure 3J). The nuclear area to basal layer area was significantly
162 increased in Het mice, with nuclei comprising most of the cellular volume (Figure 3K).

163 **Het mice exhibit delayed onset and variable progression of AAK**

164 Progression and severity of AAK were assessed by slit lamp biomicroscopy to visualize the
165 limbal region in all mice, applying the clinical grading scale for AAK (Figure 4A). In the eyes
166 of Wt mice, a transparent cornea with intact limbal border was present, and whole mount
167 staining with CD31 confirmed vessels were confined to the limbal border, representing Grade
168 0 AAK. In Het mice at one month of age, the majority (98%) had Grade 1 or 2 AAK with a
169 transparent central cornea but with vessels just breaching the limbal border and entering the
170 peripheral cornea. As Het mice age, AAK progresses with vessels entering the central cornea
171 (Grade 3) and eventually resulting in a thick, white vascularized tissue covering the entire
172 cornea (Grade 4). Relative proportions of Het mice with different AAK Grades at different
173 ages are given in Figure 4B. Notably, a large proportion of Het mice remain in early-stage
174 Grade 1-2 AAK as they age.

175 **Progressive breakdown of the corneal cellular microenvironment in AAK**

176 To investigate the impact of AAK development on the cornea at the microscopic level,
177 longitudinal in vivo imaging of mouse corneas was performed using IVCN. Epithelium
178 (superficial, wing and basal layers), stroma, and endothelium were imaged (Figure 5, A-F).
179 The large-area flat, polygonal superficial epithelial cells with bright nuclei in Wt mice (Figure
180 5A) were replaced by smaller, oval-shaped cells with dark nuclei in Het mice, that became
181 progressively smaller and less distinct as AAK progressed (Figure 5, G, L and Q). Wing cells
182 that normally have a distinct mosaic pattern with clear cell borders and dark cytoplasm and no
183 visible nuclei (Figure 5B), were transformed in Grade 1 AAK to cells with bright nuclei
184 having lost the mosaic pattern and distinct cell borders (Figure 5H), which in more advanced
185 AAK Grades completely lost all cellular structure and exhibited vacuoles (Figure 5M) and
186 fibrous material (Figure 5R). The basal cell layer of Wt mice with densely packed cells with
187 bright cell borders and dark cytoplasm (Figure 5C) with visible nerves of the subbasal
188 epithelial nerve plexus (Figure 5D) was transformed in Grade 1 AAK of Het mice to a cell

189 layer with bright nuclei and indistinct cell borders, with disrupted subbasal nerve fiber
190 orientation (Figure 5I) that in later stages lost all cellular structure (Figure 5, N and S). Bright
191 (hyper-reflective) nuclei of stromal keratocytes and thick stromal nerve fiber trunks (Figure
192 5E) in Wt mice were no longer visible in corneas of Het mice, instead being replaced by
193 fibro-vascular tissue with abnormal microneuromas (Figure 5, J, O and T). A consistent
194 monolayer of endothelial cells was visible in the normal corneal endothelium (Figure 5F) and
195 in the endothelium of Het mice, but this posterior layer became more difficult to discern with
196 increasing AAK Grade (Figure 5, K, P and U). Taken together, the results indicate a
197 progressive breakdown of the cellular and neural structure of the corneal epithelium and
198 stroma in Het mice that is discernible at the earliest stage in Grade 1 AAK when the central
199 cornea is still transparent.

200 **Het mice exhibit selective and persistent postnatal corneal lymphangiogenesis**

201 To characterize corneal neovascularization with AAK development as an indicator of
202 progressive limbal stem cell deficiency, whole mounted corneal tissues were immunostained
203 for blood (CD31) and lymphatic (LYVE1) vessels. Surprisingly in Het mice, an early and
204 selective ingrowth of corneal lymph vessels was observed at 1 month of age, extending into
205 the central cornea even without the presence of blood vessels (Figure 6A). These lymphatics
206 did not regress but persisted in the cornea to at least 5 months of age. CD31 staining revealed
207 that corneal haemangiogenesis was less prominent and delayed relative to corneal
208 lymphangiogenesis. In Wt mice, however, the cornea maintained corneal angiogenic
209 privilege, devoid of both blood and lymphatic vessels (Figure 6A, first column).
210 Blood and lymph vessel frequency was tracked over time in mice (Figure 6B) revealing that
211 lymph vessels were highly prevalent in the corneas of Het mice regardless of age, and
212 appeared to be independent of blood vessel presence, indicating that lymph vessels are more
213 dominant than blood vessels in Het mouse corneas and persist over time.

214 In the IVCN image depicted in Figure 6C, lymphatic vessels were observed coexisting with
215 blood vessels at the same corneal depth. These lymphatic vessels appear morphologically
216 distinct from adjacent blood vessels and are characterized by a larger and irregular diameter
217 compared to blood vessels. In addition, lymph vessels have no discernible vessel walls, a dark
218 lumen which is consistent with the transparency of the lymph fluid, and a few visible
219 reflective cells (presumed leukocytes) compared with blood vessels that exhibit a smaller
220 vessel diameter, thicker linear vessel walls, and a high number of small reflecting cells
221 (erythrocytes) (14).

222 Histological sections from the neovascularized area of a 2-month-old Het mouse revealed
223 LYVE1 positive vessels in the anterior corneal stroma, with additional F4/80 staining of
224 macrophages throughout the stroma. By contrast, Wt mouse corneas were devoid of both
225 LYVE1 and F4/80 positive cells (Figure 6D).

226 **Disrupted corneal nerve organization in Het mice**

227 β -III Tubulin whole mount immunostaining of corneal nerves (Figure 7) revealed that in Wt
228 mice, stromal nerves were mainly confined to the peripheral cornea with very few stromal
229 nerves in the central cornea. In contrast, in corneas of Het mice, stromal nerves extended into
230 the central cornea (Figure 7, top row). Epithelial nerve bundles derived from the peripheral
231 stromal nerve branches form a dense nerve layer called the corneal subbasal nerve plexus
232 (SBNP). In corneas of Wt mice, nerve fibers in the SBNP were densely distributed and
233 organized centripetally, converging to form a vortex at the corneal apex. In Het mice, this
234 architecture was disrupted, with an uneven and sporadic distribution of nerves in the SBNP
235 which did not exhibit any clear spatial pattern. Moreover, in the central cornea, anterior
236 stromal nerve trunks invaded the SBNP layer in the corneas of Het mice, indicating loss of
237 stromal-epithelial compartmentalization of nerves (Figure 7, bottom row).

238 **Limbal stem cell markers persist in the basal epithelium and remnants of stem-like lens**
239 **epithelium persist in the stroma of Het mice**

240 As the emergence of AAK coincides with a progressive limbal stem cell deficiency in human
241 aniridia (15), the location and distribution of limbal stem cells and differentiated epithelial
242 cells were investigated along with PAX6 expression in Het corneas in Grades 1 and 2 AAK
243 (Figure 8). In Wt mice, PAX6 was strongly expressed in all epithelial layers while in Het
244 mice, PAX6 expression was confined mainly within the flattened basal layer of the thin
245 epithelium. PAX6 expression continued to the limbal basal epithelium, where it was
246 expressed equally and uniformly in the basal cells of the limbus in Wt and Het mice. The
247 basal epithelium strongly expressed limbal stem cell marker Δ Np63 and the putative limbal
248 stem cell marker GPHA2 in the central and limbal cornea of both Wt and Het mice. The
249 superficial epithelial layer of the central cornea strongly expressed the KRT12 differentiation
250 marker in Wt and Het mice (and notably did not strongly express PAX6 or stem cell markers).
251 Superficial epithelium, however, lacked KRT12 expression in the area of keratolenticular
252 attachment in Het mice and in the limbus of both Wt and Het mice. The expression of PAX6,
253 Δ Np63, and KRT12 showed a similar pattern in Grade 3 and 4 AAK; however, GPHA2 in
254 these more advanced AAK stages shifted to the superficial epithelium (Supplementary Figure
255 S3). The proportion of Ki-67 positive cells was elevated in the basal layer of corneal epithelia
256 in Het mice compared to normal Wt tissue and became more prominent as AAK developed to
257 Grades 3 and 4. In addition, many MUC5AC-positive cells were detected in the epithelia of
258 Het mice with later-stage AAK exhibiting a uniform MUC5AC expression throughout the
259 epithelium, whereas MUC5AC expression was absent in the epithelia of Wt mice
260 (supplementary Figure S5).

261 Interestingly, within the central cornea of Het mice where the keratolenticular attachment is
262 present, clusters of cells were embedded within the corneal stroma anterior to the lens

263 capsule. These clusters exhibited a morphology distinct from the typical flattened nuclei of
264 corneal keratocytes. The positivity for stem cell markers (Δ Np63 and GPHA2) and the
265 absence of KRT12 expression within these stromal clusters imply the presence of a stem-like
266 cell population originating from the keratolenticular adhesion.

267 **Discussion**

268 AAK has been identified in almost 80% of congenital aniridia patients (2), while the
269 prevalence of a minimal keratopathy at the microscopic level has been reported to be 100% in
270 aniridia (7). AAK in human aniridia leads to significant visual morbidity and importantly,
271 there are no approved pharmacological treatments targeting its pathogenesis. An animal
272 model that closely mimics the qualities of human AAK would facilitate deeper investigations
273 of pathophysiological mechanisms and enable evaluation of potential therapies, that have
274 been previously tested in mouse models exhibiting an advanced AAK (with malformed eyes)
275 at birth (6,10,11) which makes results difficult to translate to the human disease. Here,
276 advanced in vivo imaging modalities (IVCM and OCT) alongside histopathological
277 examination were used to extensively document the dynamic structural alterations in the
278 cornea at up to five time intervals in the *Pax6*^{+/-} small eye (Sey) mouse model on the
279 129S1/SvImJ background, a model that uniquely mimics the slow-onset and progression of
280 AAK that is not seen in other Sey mouse models. In humans the natural course of AAK
281 usually begins after the first decade of life and progresses with age (7,12,15,16), a timeline
282 similar to Het mice in the present study, which importantly provides a window of up to
283 several months in mice where the central cornea remains transparent prior to AAK
284 progression. Other advantages of the present model are the time of AAK emergence and rate
285 of AAK progression. These, along with the bilateral asymmetry of AAK and even the
286 variation in phenotype across individuals, all align with various clinical observations of AAK
287 in humans (7,16). An association of AAK severity with age was found in the characterized
288 Het mice, notably with no eye having grade 0 upon careful slit lamp examination. By 1 month
289 of age, blood vessels were detected centrally or para-centrally in only 1.9 % of eyes of Het
290 mice, increasing to 26.6% of eyes by the age of 4 months. Grade 1 and 2 AAK were more
291 prominent in younger mice, while older mice mainly exhibited Grade 3 and 4 (Figure 4). This

292 corresponds to the human AAK development, where subjects under 20 years of age are
293 mostly reported with Grade 1 AAK while subjects older than 20 years usually progress to
294 Grades 2-4 (16). Our findings also demonstrated a direct correlation between the extent of
295 corneal opacification and the level of peripheral vascularization as the Het mice age,
296 consistent with observations made in humans. Although the abnormality of the epithelium in
297 aniridia has previously been documented, here we quantify several aspects of the
298 compromised epithelium in the present mouse model, that are further discussed below. At the
299 histological level, depletion of collagen IV, a prominent constituent of basement membranes,
300 was notable in Het mice. A similar reduction in collagen IV has been previously reported in
301 an aniridia patient (17), and loss of basement membrane has been noted histopathologically in
302 humans (18). The deficiency in collagen IV is expected to lead to absent or aberrant basement
303 membrane structure, disorganization of the basal layer, and a diminishment of cellular
304 demarcations, leading to fragility of the epithelium. This finding was corroborated by the
305 present in vivo findings using IVCN, where the cell borders and cellular mosaic structure
306 diminished in conjunction with advancing AAK grades. As the basement membrane provides
307 mechanical support, divides tissue into different compartments, and influences cell
308 proliferation, differentiation, and migration, the compromised basal epithelium and basement
309 membrane in Het mice, together with deficiency in the underlying Collagen IV matrix
310 structure, may result in a decline in epithelial-to-stromal barrier function. This observation
311 was confirmed by the infiltration of fluorescein dye, consistent with findings from Ou et al.'s
312 investigation on a *Pax6*^{+/-} mouse model (19). We note here also that this function may be
313 closely tied to the sparse, degenerate phenotype of the basal epithelial cells that no longer
314 appear to produce collagen IV. Moreover, presumably due to this loss of epithelial-to-stromal
315 barrier, stromal nerves migrated beyond the stromal compartment to invade the central
316 subepithelial space, replacing the normal dense spiraling network of subbasal nerves in the

317 central cornea with less dense and disorganized stromal nerve trunks. Moreover, abnormal
318 hyperproliferative stromal nerve endings called microneuromas, not detected in the corneas of
319 Wt mice, were observed in close proximity to the epithelium in Het mice, further suggesting a
320 disruption of the nerve-epithelium homeostasis. Loss of the subbasal nerve spiral pattern,
321 projection of stroma nerves into the epithelium and presence of dense ‘knotting’ of nerves
322 (microneuromas) were all noted previously by Leiper et al. in a Sey-Neu aniridia mouse
323 model (20), suggesting a compromised neurotrophic status as also observed in the present
324 model. This closely resembles the declining subbasal nerve density with age reported in
325 human studies (15,21). We note here that the neurotrophic deficit is already present in Grade
326 1 AAK, comparable to the early stages of AAK in patients (22). Moreover, the related early
327 and progressive changes in the epithelial wing and basal cell layers noted here by IVCN with
328 increasing AAK severity have also been reported in patients with aniridia (17).

329 Taken together, the compromised epithelial function and structure, along with disturbed nerve
330 organization and infiltration of inflammatory cells observed in this model, are aligned with
331 the hypothesis that perturbations in ocular surface homeostasis disrupts the vital interaction
332 between nerves and epithelial cells. This results in disruption of the normal corneal renewal
333 process, leading to an inflammatory cascade and compromised wound healing, tipping the
334 balance towards neovascularization by shifting expression of antiangiogenic factors to
335 proinflammatory and regenerative factors (1), also seen in human cases of aniridia (4,23).

336 Among inflammatory cells infiltrating the cornea, macrophages are potent triggers of
337 lymphangiogenesis due to the secretion of vascular endothelial growth factors C and D and
338 their physical incorporation within forming lymphatics (24). In the present model,
339 immunostaining revealed corneal lymph vessels accompanied by stromal infiltration of
340 F4/80⁺ macrophages. Intriguingly, we also report the currently undocumented, selective and
341 early invasion of LYVE1⁺ lymphatics into the central cornea without the presence of CD31⁺

342 blood vessels, that persisted over time in Het mice, without natural regression of these
343 vessels. This finding is notable given that the normal mouse cornea is endowed with a
344 significant number of lymphatic vessels during development, that subsequently undergo
345 spontaneous regression to the limbal area after eye opening (25). The persistence of these
346 vessels in Het mice provides further evidence for the hypothesis of a postulated frozen ocular
347 developmental state in aniridia, which also encompasses incomplete normalization of corneal
348 thickness, dendritic cell density, endothelial cell density and corneal innervation (21). This
349 suggests that inadequate levels of PAX6 could lead to the failure of spontaneous lymphatic
350 regression and thus failure of the associated postnatal corneal immune privilege. Interestingly,
351 this failure of lymphatic regression may be related to the persistence of proangiogenic
352 macrophages (24) that were observed here within the stroma of Het mice. These
353 macrophages, chronically present, may also over time contribute to blood vessel invasion of
354 the cornea and thus progression of AAK; however, given the persistent inflammation,
355 neurotrophic deficit and compromised epithelium, multiple factors likely contribute to the
356 progression of AAK.

357 AAK is often considered to be a progressive form of limbal stem cell deficiency (LSCD).
358 Immunostaining in the present model showed qualitatively that fewer epithelial cells
359 expressed LSC markers in Het mice than in wildtypes. Thus, it is plausible that a reduced
360 number of LSCs are developmentally determined in Het mice; yet, interestingly, the results
361 also show that these cells have the ability to survive for extended periods and continue to
362 express stem cell markers. However, these putative LSCs might be less efficient than
363 wildtype LSCs in terms of proliferation and producing active migrating progeny. In vivo
364 studies have also provided evidence that limbal epithelial stem cells are likely preserved in
365 human AAK (18). Moreover, visible palisades of Vogt structures in the early stages of AAK

366 have been reported, which along with preserved corneal epithelial phenotype in early stages,
367 suggests a degree of preserved LSC niche function (15,16,22).

368 Surprisingly, immunostaining results from Het mice with later-stage Grade 4 AAK also
369 revealed the persistence of limbal stem cell markers in the epithelium. Δ Np63, a well-known
370 marker for LSCs, was detected in the basal layer and supra basal epithelial layer in Wt mice
371 while in Het mice, Δ Np63 expression was confined to a single layer of flattened basal cells. In
372 Grade 4 AAK, further loss of Δ Np63 expression was apparent. Schlotzer-Schrehardt et al.
373 proposed that these cells may represent hyperproliferative transient amplifying progenitors,
374 which ensure a continuous provision and swift turnover of epithelial cells that in aniridia are
375 inadequately and aberrantly differentiated (18).

376 GPHA2 has been introduced as a new marker for quiescent stem cells (qSCs) which are
377 progenitor and slow-cycling cells surrounded by their progeny of abundant and fast-cycling
378 cells (26,27). It has also been shown that GPHA2 expression depends on niche-specific
379 signals whose function appears to be essential for LSC self-renewal and differentiation (28).
380 In Wt mice, GPHA2 was expressed in the basal epithelial layer, while in Het mice expression
381 shifted towards superficial layers of the epithelium, which was even more prominent in Grade
382 4 AAK, where expression in the basal epithelial layer was notably absent. Thus, GPHA2
383 expression in the basal epithelium appears to mirror the progressive limbal insufficiency in
384 AAK and could be an important marker for further studies.

385 The increased expression of Ki-67 in the corneal epithelium in Het mice suggests heightened
386 proliferation of progenitor cells within the basal layer, contributing to an accelerated turnover
387 of epithelial cells that are poorly differentiated, as noted above from the pattern of Δ Np63
388 expression. This leads to the development of conjunctival and epidermal phenotypes
389 evidenced by MUC5AC staining of epithelial cells found in Het mice that increased as AAK

390 progressed. Similar MUC5AC expression was found in the context of human AAK (18).
391 Previous human studies of AAK have also demonstrated a clear transformation of corneal to
392 conjunctival epithelium along with goblet cell invasion into the cornea (17,29). This suggests
393 that the epithelium in the Het mice is abnormally proliferative and transforms into
394 conjunctival epithelium that recapitulates the phenotype and progression of human AAK.

395 Of additional note, the pattern of limbal stem cell marker expression in Het mice
396 corresponded with our in vivo findings of progressive corneal opacification and
397 vascularization associated with LSCD. As observed in slit lamp images in younger mice with
398 Grades 1-2 AAK, corneal transparency is maintained implying at least partial function of the
399 limbal niche and LSCs. As AAK progressed, LSC function was compromised, resulting in
400 limbal barrier breakdown and invasion of blood vessels into the central cornea. Additionally,
401 our IVCN results showed the increasing severity of LSCD correlated with a loss of normal
402 corneal epithelial cell morphology and a decline in central subbasal nerves, in line with
403 human studies (15,30).

404 Whether the limbal stem cell function is compromised by the presence of other pathology
405 such as inflammation, neurotrophic deficit and the presence of pro-angiogenic factors is
406 unknown; however, marker expression in Het mice suggests a possibility for LSC survival,
407 potentially even in late-stage AAK. The potential for maintaining or possibly even reversing
408 the stem cell-related changes in AAK requires further exploration, and the Het mice
409 characterized here provide an excellent model for future investigations of limbal stem cell
410 biology in the context of *PAX6* transcriptional regulation. Importantly, current therapeutic
411 interventions for aniridia patients aimed at restoring the niche environment to mitigate the
412 deterioration of limbal epithelial stem cell (LESC) function are solely surgical and these have
413 proven to be largely unsuccessful (3,4).

414 Interestingly, in the region of corneas in Het mice in apposition with the kerato-lenticular
415 attachment, clusters of cells were observed embedded within the corneal stroma. These cells
416 exhibited morphological features distinct from corneal keratocytes and expressed PAX6,
417 Δ Np63 and GPHA2, but not KRT12, and are presumed lens epithelial stem-like cells, which
418 may originate from the developing prenatal lens.

419 In summary, the present Het mouse model is highly analogous to human aniridia and is the
420 only model presented to date with slow-onset AAK as observed in humans, with the cornea
421 remaining transparent for periods of up to several months. This mirrors the human AAK time
422 frame of progression according to the corresponding life cycle of mice. Phenotypic and
423 histological analyses confirmed that the complications observed in human AAK such as a
424 shallow anterior chamber, epithelial fragility, absence of Collagen IV in the epithelial
425 basement membrane, and retained hyperproliferative progenitor cells with subsequent
426 maldifferentiation of epithelial cells, are accurately recapitulated in this mouse model. In
427 addition, we note several findings in this model suitable for deeper investigation, such as
428 altered basal epithelial structure and function, persistent and selective lymphangiogenesis,
429 disrupted corneal nerve organization with microneuromas and epithelial cells with partially
430 retained stem cell markers even in late-stage AAK. There remain, however, important
431 discrepancies between our model and human AAK, namely thinner corneas in mice and
432 consistent presence of a keratolenticular adhesion. The thin cornea is common across all
433 mouse models of PAX6 deficiency (6,10,11,31). This differs notably from the thicker corneal
434 stroma in human AAK, which has been postulated to be a consequence of incomplete prenatal
435 stromal development (21). The reason for this discrepancy between mice and humans is
436 unclear and requires further investigation. The keratolenticular adhesion, present in all Het
437 mice, results from incomplete separation of the cornea and the lens during prenatal
438 development, and has been observed in other small-eye mouse models (9,10,31,32). The

439 adhesion induces a localized loss of stromal transparency at the place of attachment evident
440 even in young mice where AAK is not yet apparent and where the rest of cornea is
441 transparent. The adhesion did not appear to affect the timing or progression of vascular
442 pannus ingrowth into the cornea or the grade of keratopathy, which was notably milder than
443 in other Small-eye mouse models. The small size of the adhesion, however, permitted
444 examination of all aspects of the cornea and did not inhibit its characterization.
445 In summary, the present mouse model provides the potential to elucidate diverse
446 pathophysiologic mechanisms in the most prevalent PAX6 mutation type observed in
447 congenital human aniridia. Phenotypic features in the Het mouse cornea can provide objective
448 endpoints for future translational studies while importantly, the observed slow onset of AAK
449 provides a relevant therapeutic window for future evaluation of targeted interventions.

450 **Methods**

451 **Sex as a biological variable**

452 Both male and female mice were examined, and phenotypic findings are reported for both
453 sexes combined and separately (Table 1 and Supplementary Table S1).

454 **Animal models**

455 In this study we characterized mice of the 129S1/SvImJ background. Specifically, the
456 heterozygous 129S1.Cg-Pax6Sey/Mmmh strain (MMRRC stock number 050624-MU) with a
457 heterozygous *Pax6* mutation (11) was bred and genotyped at the animal facility of Linköpings
458 University to obtain homozygous non-mutant (*Pax6*^{+/+}, Wt) or heterozygous *Pax6* Sey mutant
459 (*Pax6*^{+/-}, Het) mice. Specifically, this mouse strain bears a spontaneous point mutation in the
460 *PAX6* gene at exon 8 (nucleotide 27726 on ENSMUSG00000027168, PAX6 mRNA
461 nucleotide 903: G to T substitution) generating a premature stop codon. For colony breeding
462 purposes, *Pax6*^{+/+} females were bred with *Pax6*^{+/-} males. Mice were housed at 23°C and 40-
463 60% humidity in a 12h/12h dark/light cycle. In total, 88 mice were characterized at various
464 age stages, comprised of 26 Het females, 16 Wt females, 24 Het males and 22 Wt males.
465 Experiments were in accordance with guidelines of the regional ethics committee for animal
466 experiments at Linköping University, Sweden and in line with the Association for Research in
467 Vision and Ophthalmology (ARVO) guidelines for the use of animals in ophthalmic and
468 vision research.

469 **Mouse genotyping and primer design**

470 To identify the mutational status of the mouse colony offspring and assign them to study
471 groups, PCR was performed on genomic DNA from digested ear clip tissue taken at weaning.
472 In order to identify the single point mutation, two pairs of primers were designed and used per
473 sample: They included a common forward primer for both pairs upstream of the mutation site,
474 and two reverse primers with an intentional penultimate base mismatch (same in both RV

475 primers, T instead of C), and an ultimate base that matched either the Wt or the Sey allele (T
476 or A, respectively). This, in the case of Wt mice, resulted in a functional Wt-RV primer with
477 one mismatch, and a non-functional Sey-RV primer with a 2-base mismatch at the 3' end,
478 giving a product only in the FW/Wt Sey primer pair. Conversely, in case of heterozygous Sey
479 mice, the FW/Wt-RV pair gave a product from the normal allele and the FW/Sey-RV pair
480 also gave a product from the mutated allele. Specifically, the primers used were: Common
481 FW: CTGTGCCGAGTCCCATTAGG, Wt RV: CTGAGCTTCATCCGAGTCTTCTTC, Sey
482 RV: CTGAGCTTCATCCGAGTCTTCTTA. DNA was extracted with 200uL 50mM NaOH
483 digestion at 90°C followed by pH neutralization by 35µL Tris-HCl (pH=8). DNA was
484 measured and 150ng of total DNA was loaded in each reaction, along with a final C of 0.5µM
485 of each primer in a reaction volume of 25µL. 12.5µL of 2x DreamTaq PCR master mix (Life
486 Technologies, ThermoFischer scientific, product # K1072) was used in each reaction that ran
487 for 35cycles of 95°C, 60°C, and 72°C.

488 **Animal anesthesia and recovery**

489 During the characterization experiments, animals were anesthetized with intra-peritoneal
490 ketamine-xylazine injection (65mg/kg ketamine, 10mg/kg xylazine in a PBS dilution for
491 10µL per g of weight injection) and topical anesthesia of tetracaine-HCl 0.5% drops was also
492 applied. At the end of the characterization, if the timepoint was not terminal, mice were
493 administered 1.8mg/Kg in PBS atipamezole subcutaneously in the back and were allowed to
494 wake up in a cage with paper bedding, warmed by warm pads. For analgesia, 0.12mg/Kg
495 buprenorphine was included in the antisedan solution (injectable solution concentration:
496 0.225mg/mL atipamezole, 0.015mg/mL buprenorphine).

497 **Characterization of mice**

498 Characterization was performed on both eyes per mouse at 5 time points with 1-month
499 intervals starting at the age of 1 month to 5 months of age using slit-lamp photography, IVC

500 imaging of corneal layers and Optical Coherence Tomography. At every timepoint, after the
501 characterization of all eyes, 2 Het mice and 2 Wt mice were taken out of their groups and
502 sacrificed for tissue extraction, while all other animals were kept in their housing until
503 reaching the next age timepoint. Obtained tissues were dissected, processed or preserved
504 according to the specific assay for which they were individually allocated. The specific assays
505 and the corresponding tissue handling after extraction are described below in their respective
506 sections. A clinical grading scale for AAK was applied to all Het mice, as previously reported
507 (7). Briefly, Grade 0 AAK is a complete and undamaged limbal border indistinguishable from
508 a healthy corneal limbus, Grade 1 AAK is where blood vessels cross the limbus while
509 remaining within 1 mm of the limbal area, Grade 2 AAK is where blood vessels invade the
510 peripheral and paracentral cornea, but preserving the central 2 mm of the cornea, Grade 3
511 AAK is characterized by vascularization affecting the central cornea and Grade 4 is an
512 advanced end-stage AAK with vascularization of the entire cornea and transformation of the
513 anterior cornea into an opaque, thick, white, vascularized irregular structure.

514 **Slit-lamp photography**

515 Mouse eyes were examined using a rodent slit-lamp camera (Micron III, Phoenix
516 Technologies, USA) for visualization and scoring of corneal haze and opacity. After initial
517 slit-lamp photography, 5mg/mL Tropicamide drops were applied for 4min to dilate the iris
518 and the eyes were re-photographed after rinsing of the tropicamide drops with PBS eye drops.
519 Corneal haze grading was assessed by slit lamp examination at each time point using a
520 previously reported grading scale (33).

521 **In Vivo Confocal Microscopy (IVCM) imaging of corneal layers**

522 In vivo confocal microscopy (Heidelberg Retinal Tomograph 3 with Rostock Corneal
523 Module, HRT3-RCM, Heidelberg Engineering, Germany) was used to image the corneal
524 layers to detect possible lesions, abnormal features and inflammatory cell infiltrates while

525 also visualizing the corneal nerve plexus. After application of viscotears gel (2mg/g
526 polyacrylic acid), the laser head was brought in close contact with the cornea epithelium and
527 images were obtained and recorded throughout the corneal layers.

528 **Optical Coherence Tomography**

529 The Optovue iVue-100 OCT system with a corneal adaptor module was used on both eyes per
530 mouse using the iVue system in the corneal pachymetry mode. The Fourier-domain OCT
531 device operates at a scanning speed of 26000 A-scans per second with a frame rate of 256 to
532 4096 A-scans per frame. The axial and transverse resolutions of the iVue-100 OCT device are
533 5 μm and 15 μm respectively (manual).

534 **Cornea tissue sample processing**

535 Upon sacrifice, eye bulbs were extracted with forceps. For histology, the whole eye was
536 rinsed in PBS and immersed in 4% PFA in PBS at 4°C 2 hours, rinsed thoroughly with PBS
537 and kept in ethanol 70%. After being embedded in paraffine blocks, they were sectioned at 5
538 μm thickness, mounted to poly-L lysine coated microscopy slides, dried overnight at RT and
539 further processed for histological-immunohistological-IF staining. In all other cases, the
540 cornea was separated immediately and washed with ice-cold PBS. For protein analysis, the
541 cornea was immersed in 80 μL RIPA buffer (Thermo-Scientific 89901) supplemented with
542 protease and phosphatase inhibitors with 5mM EDTA (Thermo-Scientific Halt™ 78442) ,
543 then was snap frozen and stored at -80°C. For whole mount staining the corneas after being
544 immersed in 1.3% PFA at 4°C 1 hour, were kept in PBS for staining.

545 **Immunostaining and confocal fluorescence microscopy**

546 Sections from Het mice corneas including the attachment were excluded from quantitative
547 analyses to minimize the probable effect of attachment on the corneal phenotype outside the
548 attachment zone. A standard protocol for section rehydration, antigen retrieval, blocking and
549 antibody staining was used. Briefly, antigen retrieval was performed in the DAKO PT LINK

550 200 machine, nonspecific epitope blocking was performed by 1% BSA (Sigma-Aldrich via
551 Merck #A7906) , 5% goat serum (Cell Signaling via BioNordika #CST-5425S), 0.1% Tween-
552 20 in PBS, primary ab was incubated overnight at 4°C, secondary antibodies were applied for
553 2h at RT and SlowFade™ Diamond Antifade mountant with DAPI (Fischer scientific #
554 15451244) were used to mount immunostained slides or Eukitt quick-hardening mounting
555 medium (Sigma-Aldrich via Merck #03989) for IHC-stained slides. We specifically examined
556 ΔNp63 and GPHA2 as indicators for limbal stem cells (LSC), in addition to KRT12 as a
557 marker for differentiated epithelial cells (negative marker for stem cells). For completeness,
558 images were taken of the central cornea including and excluding regions of keratolenticular
559 adhesions in Het mice. For whole-mounts, corneas were cut into 4 leaflets and then
560 proceeded to immunofluorescence protocol. Briefly, after nonspecific epitopes being blocked
561 for 1 hour, the corneas were incubated in primary antibody overnight. Fluorophore-
562 conjugated secondary antibodies were applied for 2 nights. A Zeiss LSM 800 microscope
563 (Carl Zeiss AG, Oberkochen, Germany) was used for imaging. Antibodies used are listed in
564 the table provided in the supplementary Table S2.

565

566

567 **Western blot**

568 For protein extraction, samples were homogenized using the TissueLyser LT bead mill
569 system (Qiagen) at 50Hz shaking for 5min, followed by sonication in ice-cold water for
570 10min and a 20min centrifugation step. Protein concentration was measured using the
571 Pierce™ BCA Protein Assay kit (Thermo-Scientific) following the instructions for a 10µL
572 sample volume. BIS-polyacrylamide gel electrophoresis was performed using 4-15% gradient
573 pre-cast gel (Bio-Rad #4561084 Mini-PROTEAN® TGX™). 15µg total protein per sample
574 were loaded, mixed with 4x Laemmli buffer (Bio-Rad #1610747), 0.5µL β-mercaptethanol
575 and ddH2O. Proteins were transferred in a PVDF membrane using Trans-Blot Turbo Mini 0.2
576 µm PVDF Transfer Packs (Bio-Rad #1704156) and standard membrane immunostaining
577 procedures were followed, detailed in the supplementary methods. Bands were visualized in
578 an ImageQuant™ LAS 500 Chemiluminescent Imaging System (GE Healthcare), after being
579 covered by 1mL of Pierce™ ECL Western Blotting Substrate (Thermo Fisher #32106). Band
580 densitometry on the photographed membranes was performed using the Image Lab v.6.1
581 software (Bio-Rad Laboratories).

582 **Quantitative measurements and statistics**

583 ImageJ software (version 1.54, FIJI distribution) was utilized for all morphometric
584 measurements of various aspects of microscopy images (34). Measurements in OCT images
585 were performed within the OCT built-in software (v 3.2.1.8). Prism v.8.3.0 (GraphPad
586 Software) was used for the statistical evaluation in group comparisons and to produce charts.
587 Multiple samples were compared using one-way ANOVA followed by post-hoc Tukey
588 multiple comparison tests. Results were reported as mean ± standard error of mean (SEM). p-
589 value of 0.05 or less was considered significant. For statistical comparisons for the frequency

590 of phenotypic findings between sexes, IBM SPSS version 29.0.2.0 (IBM Corp.) software was
591 used with the Chi-square method with continuity correction and Bonferroni adjustment for
592 multiple testing.

593 **Study approval**

594 Animal procedures were approved by the Linköping Regional Animal Ethics review board
595 (Application Nos. 10940-2021, 06826-2024).

596 **Data availability**

597 All relevant data along with raw measurements of all parameters have been provided in the
598 manuscript or in the supplementary information (see ‘Supporting Data Values’ supplementary
599 Excel file). All measurements are presented individually for each experiment sample.

600 Libraries of microscopy photos are available from the corresponding author upon reasonable
601 request with no restrictions on data availability.

602 **Author contributions**

603 DJ: Performed experiments, data acquisition, tissue processing, interpretation and drafted the
604 manuscript. PM: Performed experiments, data and tissue processing, interpretation, image
605 preparation, partial writing and review of the manuscript. MA: Performed tissue processing
606 and analysis and review of the manuscript. AD: Performed imaging and assisted with image
607 processing, tissue processing, and review of the manuscript. YR: Performed image analysis
608 and review of the manuscript. NL: Conceptualization, study design, design and coordination
609 of experiments, funding, data interpretation, assisted with manuscript writing and critical
610 manuscript review and revisions.

611 **Acknowledgments**

612 This project was funded by the European Union through the European Joint Programme on
613 Rare Diseases (EJPRD) under the project AAK-INSIGHT, Grant No. EJPRD20-135. We
614 thank Elizabeth Simpson from the University of British Columbia, Vancouver, Canada, for

615 developing and providing the Sey mice on the 129S1/SvImJ background to the Mutant Mouse
616 Resource and Research Center at the Jackson Laboratories. The authors wish to also thank
617 Meri Vattulainen for technical assistance with procurement and preparation of prenatal
618 corneal tissue sections.

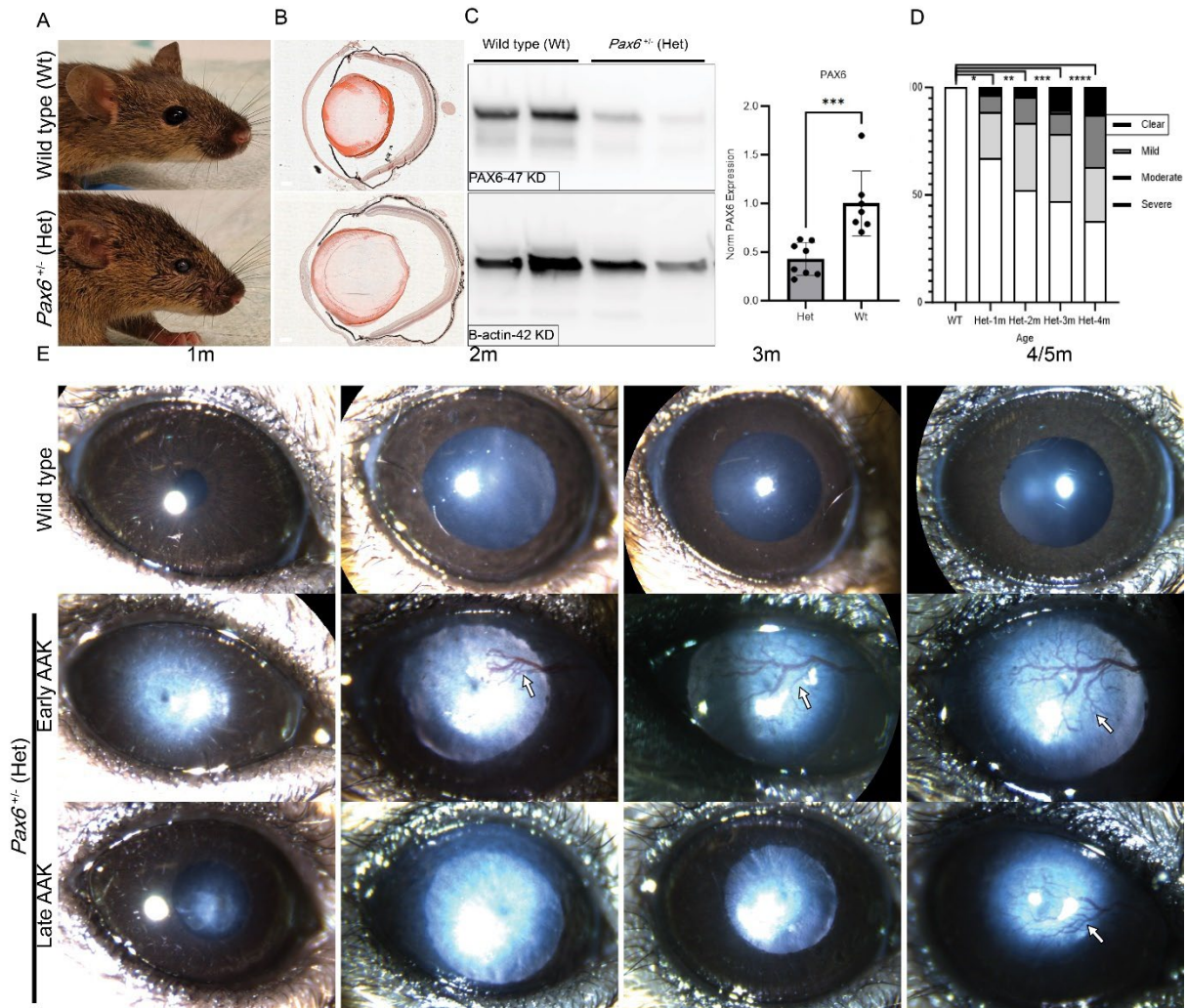
619 **References**

- 620 1. Latta L, et al. Pathophysiology of aniridia-associated keratopathy:
621 Developmental aspects and unanswered questions. *Ocul Surf.* Oct 2021;22:245-266.
622 doi:10.1016/j.jtos.2021.09.001
- 623 2. Landsend ECS, et al. Congenital aniridia - A comprehensive review of clinical
624 features and therapeutic approaches. *Surv Ophthalmol.* Nov-Dec 2021;66(6):1031-1050.
625 doi:10.1016/j.survophthal.2021.02.011
- 626 3. Behaegel J, et al. Outcomes of Human Leukocyte Antigen-Matched Allogeneic
627 Cultivated Limbal Epithelial Transplantation in Aniridia-Associated Keratopathy-A Single-
628 Center Retrospective Analysis. *Cornea.* Jan 1 2022;41(1):69-77.
629 doi:10.1097/ico.0000000000002729
- 630 4. van Velthoven AJH, et al. Future directions in managing aniridia-associated
631 keratopathy. *Surv Ophthalmol.* Sep-Oct 2023;68(5):940-956.
632 doi:10.1016/j.survophthal.2023.04.003
- 633 5. Kit V, et al. Longitudinal genotype-phenotype analysis in 86 patients with
634 PAX6-related aniridia. *JCI Insight.* Jul 22 2021;6(14)doi:10.1172/jci.insight.148406
- 635 6. Gregory-Evans CY, et al. Postnatal manipulation of Pax6 dosage reverses
636 congenital tissue malformation defects. *J Clin Invest.* Jan 2014;124(1):111-6.
637 doi:10.1172/jci70462
- 638 7. Lagali N, et al. PAX6 Mutational Status Determines Aniridia-Associated
639 Keratopathy Phenotype. *Ophthalmology.* Feb 2020;127(2):273-275.
640 doi:10.1016/j.ophtha.2019.09.034
- 641 8. Lima Cunha D, et al. Restoration of functional PAX6 in aniridia patient iPSC-
642 derived ocular tissue models using repurposed nonsense suppression drugs. *Mol Ther Nucleic*
643 *Acids.* Sep 12 2023;33:240-253. doi:10.1016/j.omtn.2023.06.016
- 644 9. Wang X, et al. Efficacy of Postnatal In Vivo Nonsense Suppression Therapy in a
645 Pax6 Mouse Model of Aniridia. *Mol Ther Nucleic Acids.* Jun 16 2017;7:417-428.
646 doi:10.1016/j.omtn.2017.05.002
- 647 10. Rabiee B, et al. Gene dosage manipulation alleviates manifestations of
648 hereditary PAX6 haploinsufficiency in mice. *Sci Transl Med.* Dec 9
649 2020;12(573)doi:10.1126/scitranslmed.aaz4894
- 650 11. Hickmott JW, et al. Epistasis between Pax6(Sey) and genetic background
651 reinforces the value of defined hybrid mouse models for therapeutic trials. *Gene Ther.* Dec
652 2018;25(8):524-537. doi:10.1038/s41434-018-0043-6
- 653 12. Fries FN, et al. Early ocular surface and tear film status in congenital aniridia
654 indicates a supportive treatment window. *Br J Ophthalmol.* Dec 18 2023;108(1):30-36.
655 doi:10.1136/bjo-2021-320774
- 656 13. Saito K, et al. Distribution of α (IV) collagen chains in the ocular anterior
657 segments of adult mice. *Connect Tissue Res.* Apr 2011;52(2):147-56.
658 doi:10.3109/03008207.2010.492062
- 659 14. Peebo BB, et al. Cellular-level characterization of lymph vessels in live,
660 unlabeled corneas by in vivo confocal microscopy. *Invest Ophthalmol Vis Sci.* Feb
661 2010;51(2):830-5. doi:10.1167/iovs.09-4407
- 662 15. Lagali N, et al. In vivo morphology of the limbal palisades of vogt correlates
663 with progressive stem cell deficiency in aniridia-related keratopathy. *Invest Ophthalmol Vis*
664 *Sci.* Aug 7 2013;54(8):5333-42. doi:10.1167/iovs.13-11780
- 665 16. Lagali N, et al. Stage-related central corneal epithelial transformation in
666 congenital aniridia-associated keratopathy. *Ocul Surf.* Jan 2018;16(1):163-172.
667 doi:10.1016/j.jtos.2017.11.003

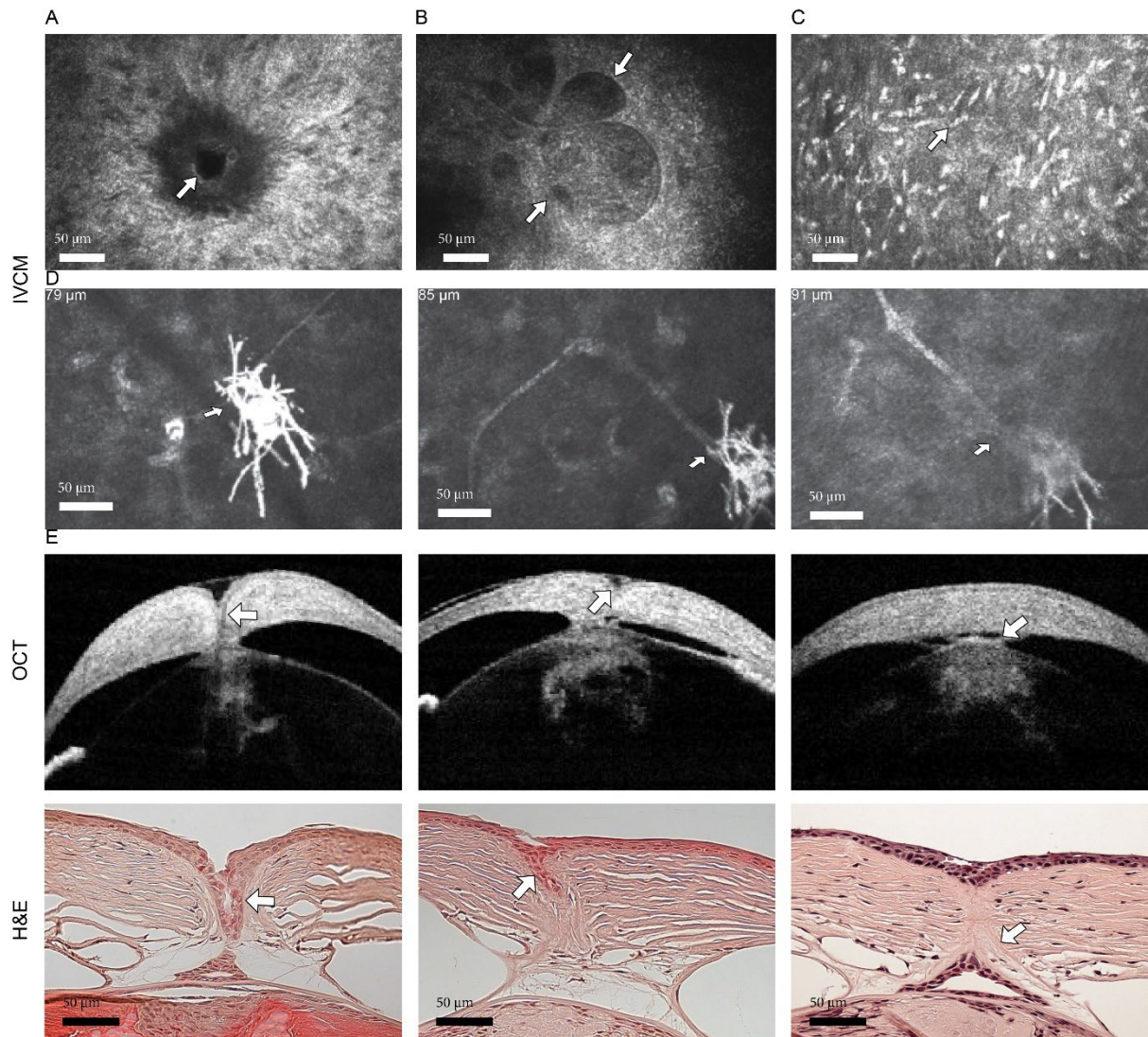
- 668 17. Ihnatko R, et al. Congenital Aniridia and the Ocular Surface. *Ocul Surf.* Apr
669 2016;14(2):196-206. doi:10.1016/j.jtos.2015.10.003
- 670 18. Schlötzer-Schrehardt U, et al. Dysfunction of the limbal epithelial stem cell
671 niche in aniridia-associated keratopathy. *Ocul Surf.* Jul 2021;21:160-173.
672 doi:10.1016/j.jtos.2021.06.002
- 673 19. Ou J, et al. Chronic wound state exacerbated by oxidative stress in Pax6+/-
674 aniridia-related keratopathy. *J Pathol.* Aug 2008;215(4):421-30. doi:10.1002/path.2371
- 675 20. Leiper LJ, et al. Control of patterns of corneal innervation by Pax6. *Invest*
676 *Ophthalmol Vis Sci.* Mar 2009;50(3):1122-8. doi:10.1167/iovs.08-2812
- 677 21. Lagali N, et al. Early phenotypic features of aniridia-associated keratopathy and
678 association with PAX6 coding mutations. *Ocul Surf.* Jan 2020;18(1):130-140.
679 doi:10.1016/j.jtos.2019.11.002
- 680 22. Edén U, et al. Pathologic epithelial and anterior corneal nerve morphology in
681 early-stage congenital aniridic keratopathy. *Ophthalmology.* Sep 2012;119(9):1803-10.
682 doi:10.1016/j.ophtha.2012.02.043
- 683 23. Latta L, et al. Abnormal neovascular and proliferative conjunctival phenotype in
684 limbal stem cell deficiency is associated with altered microRNA and gene expression
685 modulated by PAX6 mutational status in congenital aniridia. *Ocul Surf.* Jan 2021;19:115-127.
686 doi:10.1016/j.jtos.2020.04.014
- 687 24. Maruyama K, et al. Inflammation-induced lymphangiogenesis in the cornea
688 arises from CD11b-positive macrophages. *J Clin Invest.* Sep 2005;115(9):2363-72.
689 doi:10.1172/jci23874
- 690 25. Zhang H, et al. Spontaneous lymphatic vessel formation and regression in the
691 murine cornea. *Invest Ophthalmol Vis Sci.* Jan 2011;52(1):334-8. doi:10.1167/iovs.10-5404
- 692 26. Altshuler A, et al. Eyes open on stem cells. *Stem Cell Reports.* Dec 12
693 2023;18(12):2313-2327. doi:10.1016/j.stemcr.2023.10.023
- 694 27. Altshuler A, et al. Discrete limbal epithelial stem cell populations mediate
695 corneal homeostasis and wound healing. *Cell Stem Cell.* Jul 1 2021;28(7):1248-1261.e8.
696 doi:10.1016/j.stem.2021.04.003
- 697 28. Collin J, et al. A single cell atlas of human cornea that defines its development,
698 limbal progenitor cells and their interactions with the immune cells. *Ocul Surf.* Jul
699 2021;21:279-298. doi:10.1016/j.jtos.2021.03.010
- 700 29. Nishida K, et al. Ocular Surface Abnormalities in Aniridia. *American Journal of*
701 *Ophthalmology.* 1995/09/01/ 1995;120(3):368-375. doi:[https://doi.org/10.1016/S0002-](https://doi.org/10.1016/S0002-9394(14)72167-1)
702 [9394\(14\)72167-1](https://doi.org/10.1016/S0002-9394(14)72167-1)
- 703 30. Deng SX, et al. Characterization of limbal stem cell deficiency by in vivo laser
704 scanning confocal microscopy: a microstructural approach. *Arch Ophthalmol.* Apr
705 2012;130(4):440-5. doi:10.1001/archophthalmol.2011.378
- 706 31. Ramaesh T, et al. Corneal abnormalities in Pax6+/- small eye mice mimic
707 human aniridia-related keratopathy. *Investigative ophthalmology & visual science.*
708 2003;44(5):1871-1878.
- 709 32. Kanakubo S, et al. Abnormal migration and distribution of neural crest cells in
710 Pax6 heterozygous mutant eye, a model for human eye diseases. *Genes to Cells.*
711 2006;11(8):919-933.
- 712 33. Hanna KD, et al. Corneal Wound Healing in Monkeys After Repeated Excimer
713 Laser Photorefractive Keratectomy. *Archives of Ophthalmology.* 1992;110(9):1286-1291.
714 doi:10.1001/archopht.1992.01080210104035
- 715 34. Schindelin J, et al. Fiji: an open-source platform for biological-image analysis.
716 *Nature methods.* 2012;9(7):676-682.

- 717 35. Dutta S, Sengupta P. Men and mice: Relating their ages. *Life Sci.* May 1
718 2016;152:244-8. doi:10.1016/j.lfs.2015.10.025
- 719 36. Flurkey K, et al. Chapter 20 - Mouse Models in Aging Research. In: Fox JG,
720 Davisson MT, Quimby FW, Barthold SW, Newcomer CE, Smith AL, eds. *The Mouse in*
721 *Biomedical Research (Second Edition)*. Academic Press; 2007:637-672.
722

Table 1. Frequency of abnormalities in <i>Pax6</i> ^{+/-} 129S1/SvImJ heterozygous mice				
Age	1 month n=52	2 months n=42	3 months n=32	4 months n=60
Approximate human age translation (source 1) (35)	8 years	23 years	34 years	46 years
Approximate human age translation (source 2) (36)	12-17	>17 years	20-30, towards young range	20-30, mid-range
Sex	F=30, M=22	F=24, M=18	F=18, M=14	F=28, M=32
Keratolenticular adhesion	52 (100%)	42 (100%)	32 (100%)	60 (100%)
Iris coloboma	23 (44,2%)	22 (52,3%)	14 (43,7%)	23 (38,3%)
Cornea				
Inflammatory cells	11 (21,1%)	14 (33,3%)	5 (15,6%)	4 (6,6%)
Neuroma	32 (61,5%)	28 (66,6%)	19 (59,3%)	46 (76,6%)
Vacuole structure	21 (40,3%)	15 (35,7%)	11 (34,3%)	15 (25%)
Values given indicate number (n) of eyes of Het mice with percentages of the total number at that age given in parentheses. F = female, M = male.				

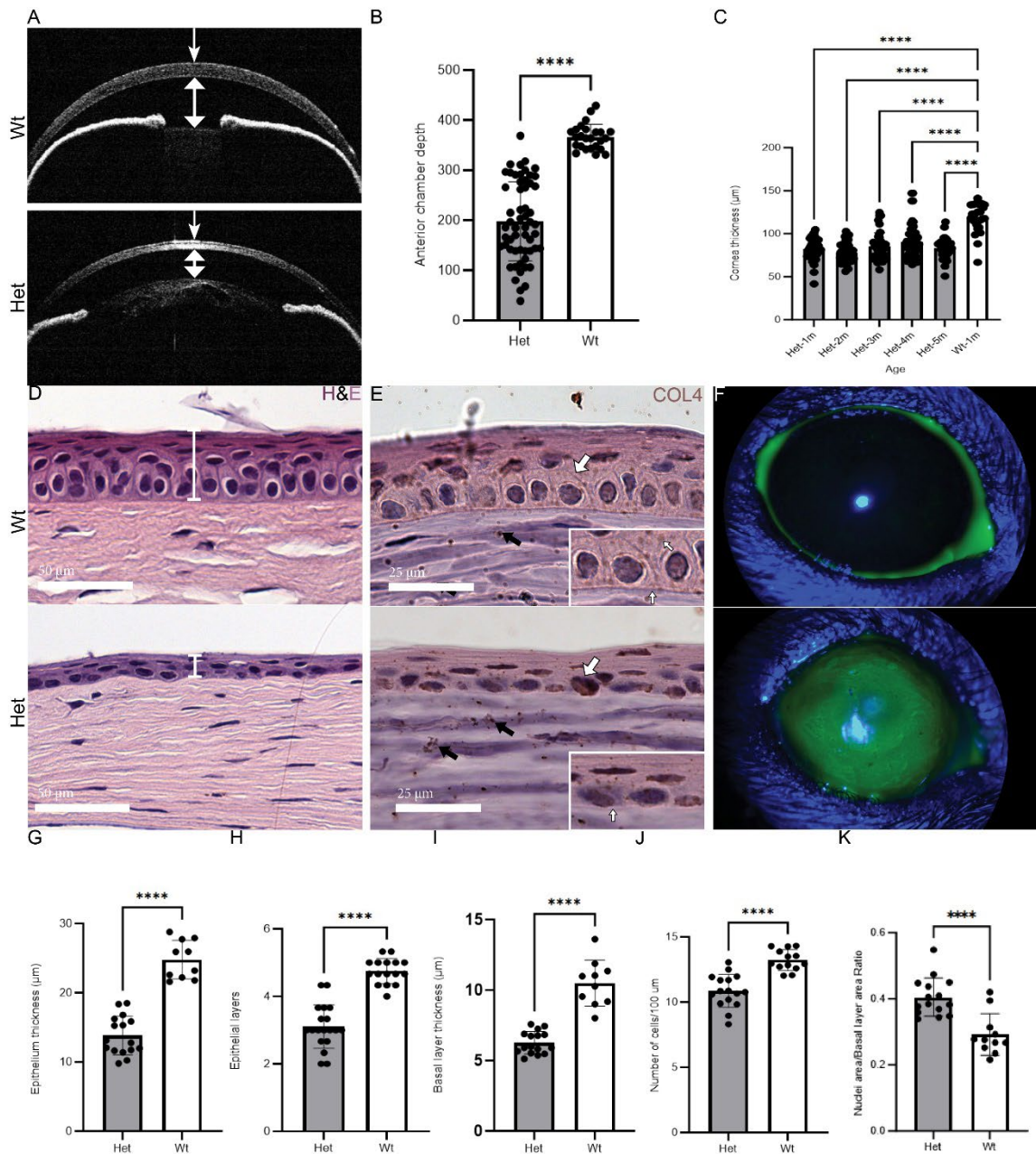


726
 727 **Figure 1.** The *Pax6*^{+/-} 129S1/SvImJ mouse model phenotype mimicking the variable onset of
 728 human AAK caused by PAX6 haploinsufficiency. (A) Representative images of a Wt and Het
 729 mouse head showing only slightly smaller and less bulging eyes. (B) Hematoxylin and eosin
 730 staining reveals an underdeveloped anterior segment in Het mice. Scale bar= 200 μ m. (C)
 731 Western blot analysis indicates a significant 58% decrease in PAX6 protein levels in corneas
 732 from Het mice compared to Wt littermates, $n > 7$ (t-test ***: $P < 0.001$). (D) Longitudinal
 733 characterization over a period of 5 months indicates a gradual and distributed pattern of loss
 734 of corneal transparency, $n > 32$ (Kruskal-Wallis test ****: $P < 0.0001$, group comparisons *
 735 for $P < 0.05$, ** for $P < 0.01$, *** for $P < 0.001$ and **** for $P < 0.0001$). (E) Slit lamp
 736 analysis revealed unchanged cornea status in Wt mice and early and late AAK onset
 737 phenotypes in Het mice, both being progressive.
 738

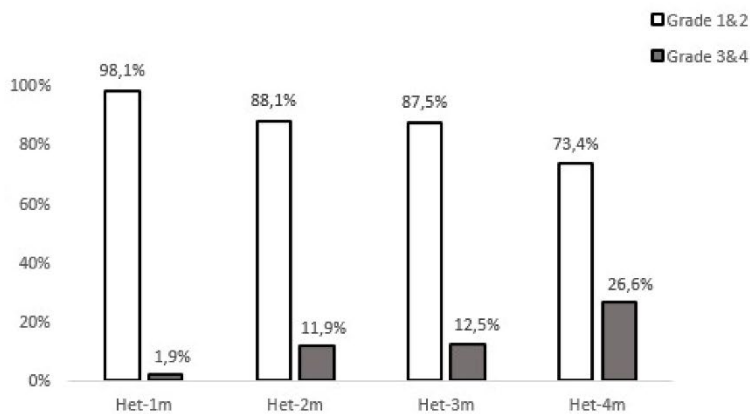
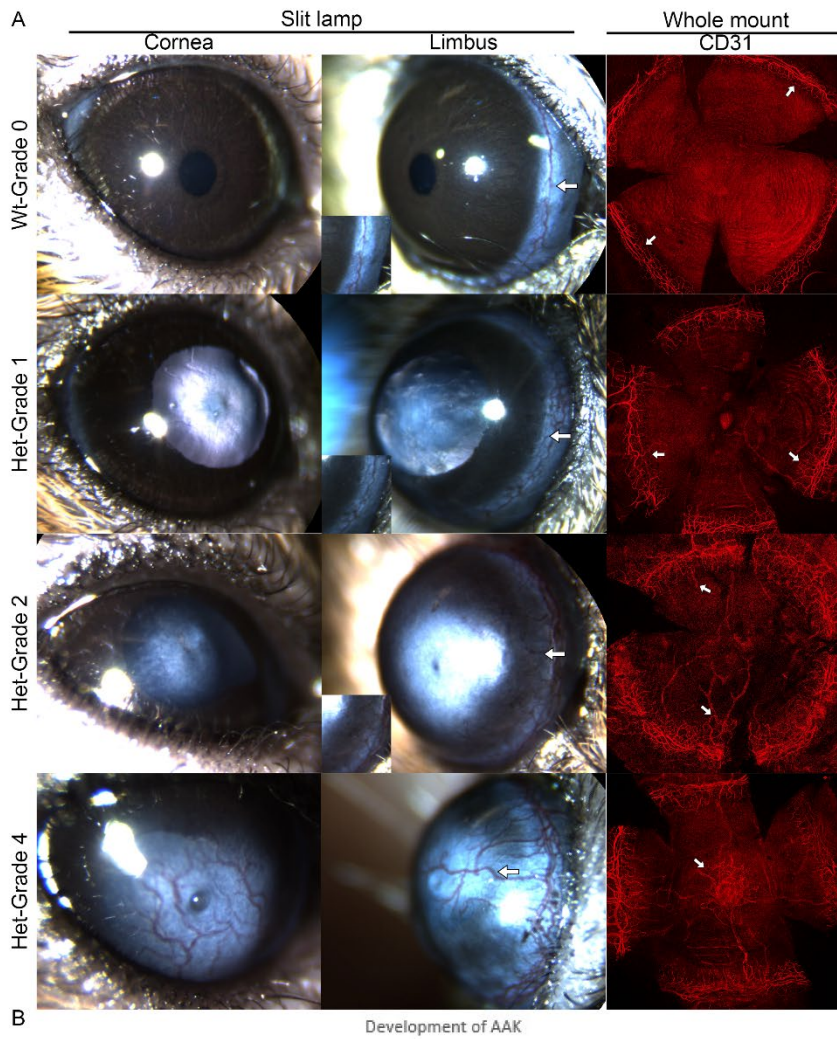


739
740
741
742
743
744
745
746
747
748

Figure 2. Corneal microstructural abnormalities Het mice. (A) Point of keratolenticular adhesion in the posterior corneal stroma (arrow). (B) Dark vacuole structures (arrows) in the posterior corneal stroma. (C) Infiltration of inflammatory cells (arrow) in the corneal stroma. (D) Serial IVCM sections at different depths indicating the presence of a neuroma (arrows) and the attachment point to a stromal nerve trunk (arrows). (E) In vivo images of different degrees of keratolenticular adhesions by OCT (top row), with lens material indicated by arrows, and the corresponding H&E staining from the same eye, indicating the lens cells within the cornea (arrows, bottom row).



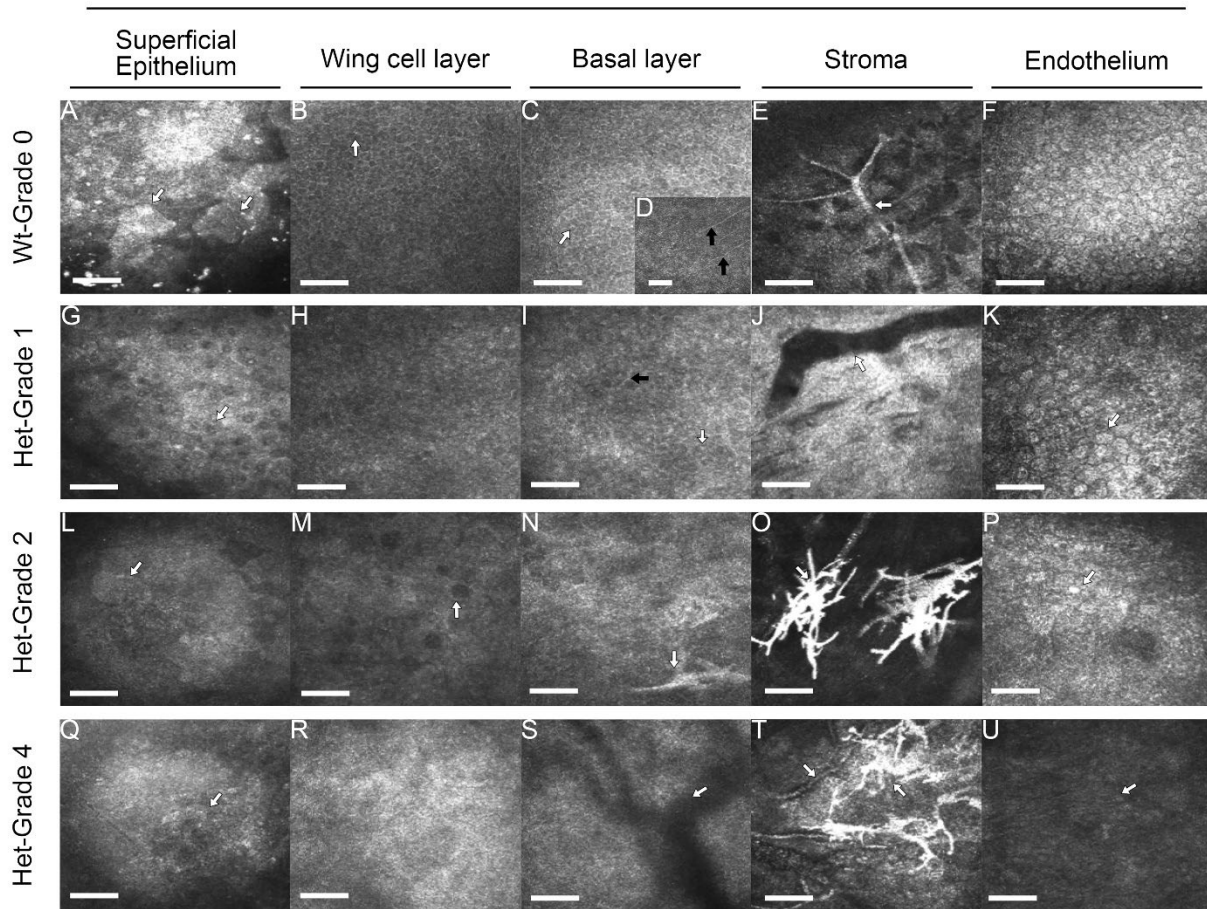
749
 750 **Figure 3.** Corneal and epithelial structural abnormalities in Het mice. (A) OCT images of Wt and Het
 751 mouse eyes indicating thinner corneas and shallower anterior chamber depth in Het mice. (B) Anterior
 752 chamber depth is reduced by half in Het mice, n>25. (C) Central corneal thickness measured in vivo
 753 with OCT indicated significantly thinner corneas in Het mice not changing with age, n>25. (D)
 754 Representative H&E images of corneas from Het and Wt mice revealing thinner epithelium (marked)
 755 in Het mice. (E) COL4 DAB staining revealed absence of COL4 production in basal epithelial cells
 756 and absent epithelial basement membrane in Het mice (Inset, white arrows), and dot-like expression of
 757 COL4 in the stroma representing basement membrane surrounding corneal nerves (black arrows). (F)
 758 Fluorescein staining indicated compromised epithelial barrier function with stromal uptake of the dye
 759 in vivo. (G-K) Comparative analysis from H&E images from Het (n=16) and Wt mice (n>10). (G)
 760 Epithelium thickness, n>10. (H) Number of epithelial layers, n>17. (I) Basal layer thickness, n>10. (J)
 761 Number of basal cells per 100 μm linear distance, n > 13. (K) Nuclear area-to-basal layer area ratio in
 762 basal cells, n>11. In all panels **** indicates p < 0.0001 (t-test in two-group panels or ANOVA
 763 multiple pairwise comparison).
 764



765
766
767
768
769
770
771

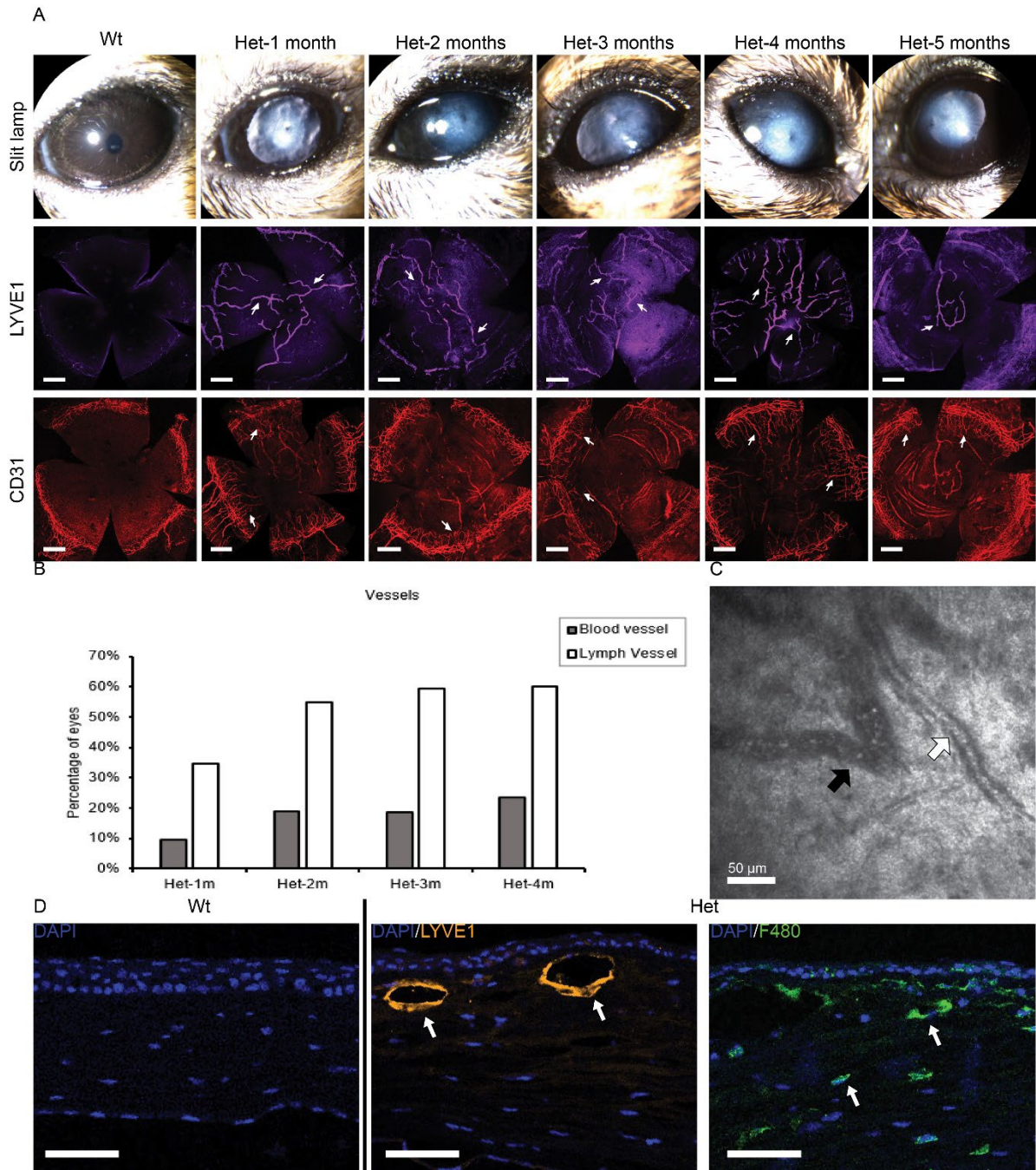
Figure 4. Grade and progression of AAK in Het mice. (A) Representative slit lamp images from 1 or 2 mice of each Grade and whole-mount staining with CD31 for each Grade, indicating different Grades of AAK. In Wt mice, arrows indicate the intact limbal border. In Het mice, arrows indicate blood vessels that have just breached the limbal border and entered the cornea. (B) Distribution of AAK grade among Het mice of different ages, n > 32.

IVCM

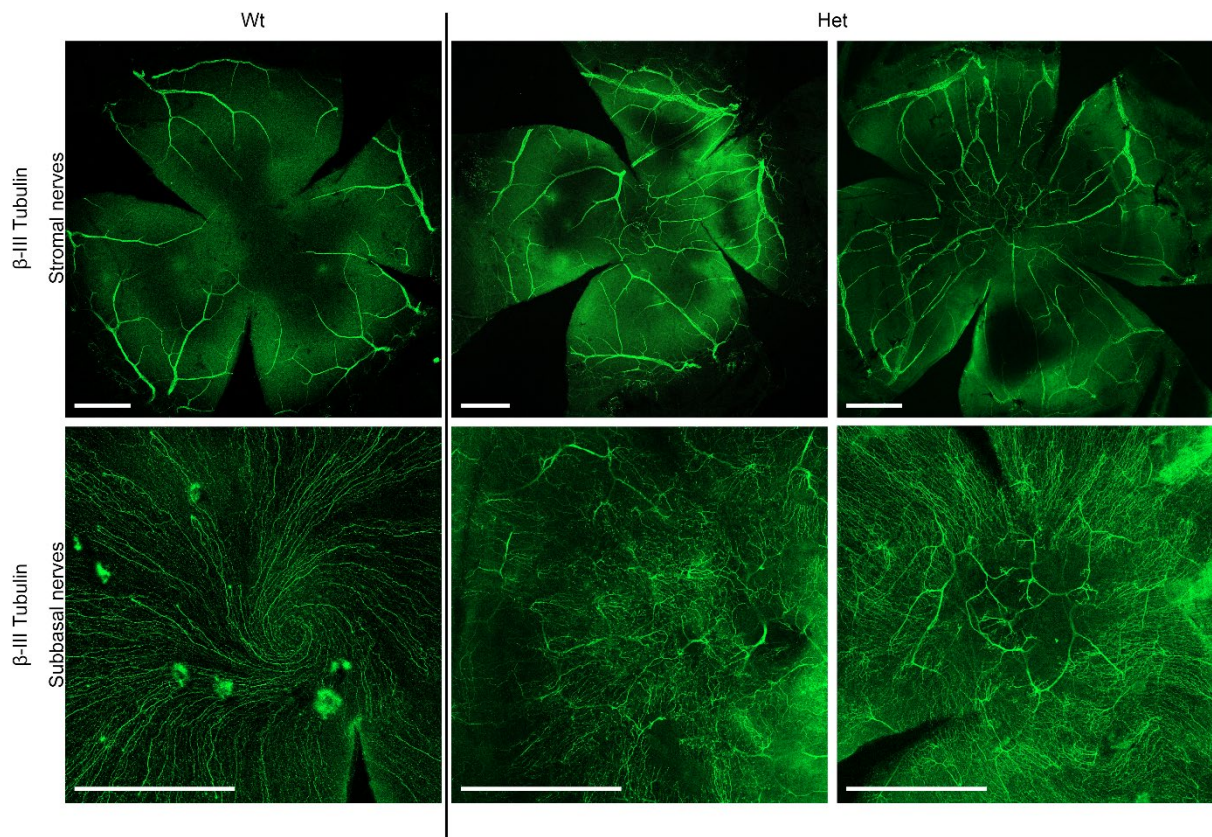


772
773
774
775
776
777
778
779
780
781
782
783
784
785
786
787
788
789
790

Figure 5. Longitudinal in vivo examination of corneal microstructure with IVCM. (First row) Normal corneal cellular layers in Wt mice. (A) Polygonal flat (arrow) superficial epithelial cells. (B) Wing cell layer with bright borders and dark cytoplasm (arrow). (C) Basal cell layer with bright borders and densely packed cells (arrow). (D) Network of subbasal nerves within a dense nerve plexus (black arrows). (E) Branching stromal nerve fiber trunk (arrow). (F) Hexagonal monolayer of endothelial cells. (Second row) cornea layers in Grade 1 AAK. (G) Superficial cells are small, non-polygonal and with dark nuclei (arrow). (H) Loss of distinct mosaic pattern and loss of dark cytoplasm of wing cells. (I) The parallel and regular pattern of subbasal nerves is disrupted (black arrow). (J) Vascular structure in the stroma. (K) Visible endothelial cells (arrow). (Third row) Cornea layers in Grade 2 AAK. (L) Indistinct superficial epithelial cells (arrow). (M) Dark vacuole-like structure (arrow) and loss of cellular mosaic. (N) Loss of distinct cellular structure, with neuroma visible that approaches the basal layer (arrow). (O) Large hyper-reflective neuromas (arrow) in stroma. (P) Indistinct hexagonal endothelial cell (arrow). (Fourth row) Cornea layers in Grade 4 AAK. (Q) Very small superficial cells (arrow). (R) Fibrous tissue replacing the wing cell layer. (S) Shadows of stromal vessels (arrow) at the level of the basal layer. (T) Co-appearance of vessels and neuromas in stroma (arrows). (U) Faintly detectable nuclei (arrow) of endothelial cells. Scale bars = 50 μ m.

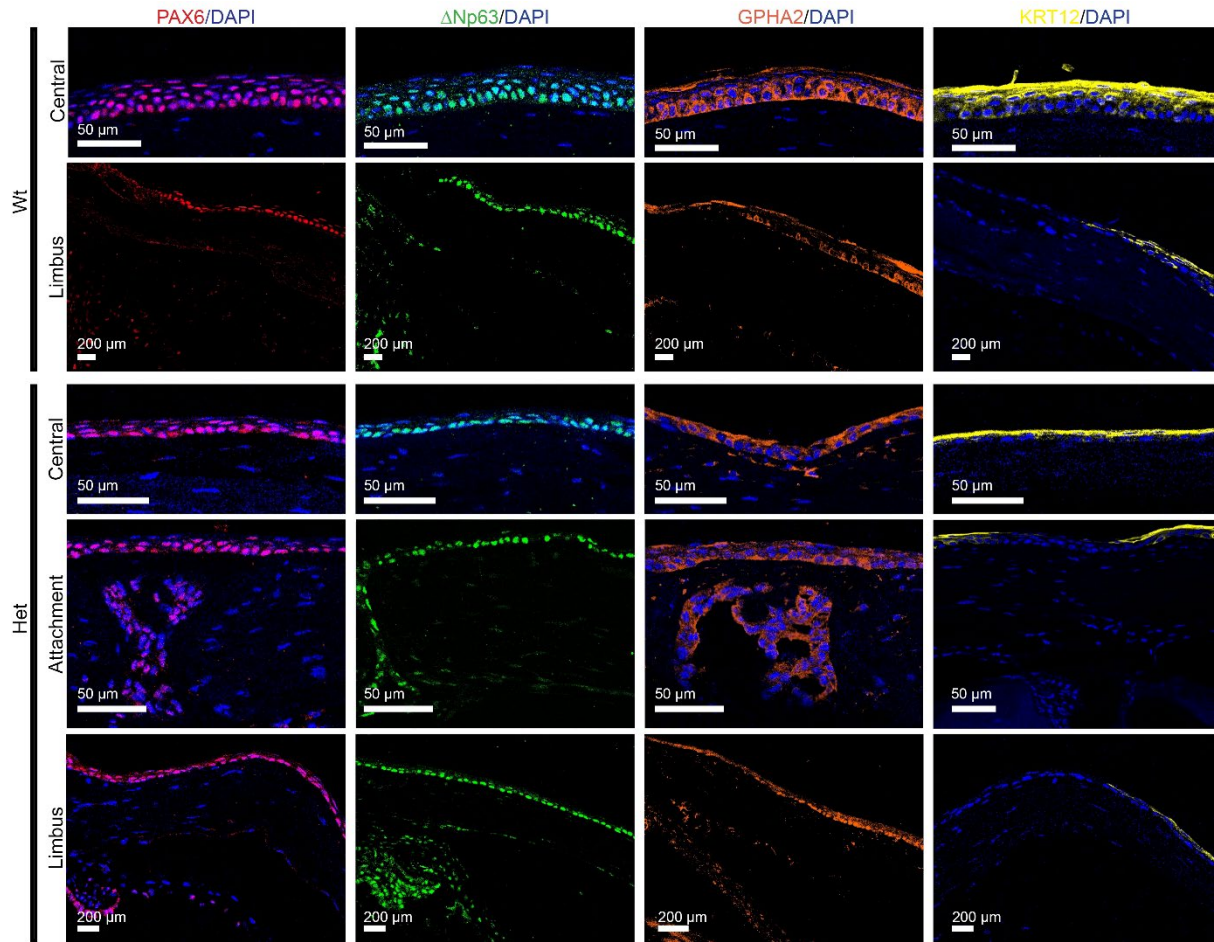


791
 792 **Figure 6.** Time course and characteristics of corneal neovascularization. (A) Slit lamp images
 793 (top row) confirming Grade 1 and 2 AAK in Het mice up to the age of 5 months. Corresponding
 794 whole-mounted corneas immunostained for lymph vessels (LYVE1, middle row) and blood
 795 vessels (CD31, bottom row). White arrows in both rows highlight lymph and blood vessels,
 796 respectively. Sale bar= 500 μm (B) Prevalence of corneal lymph vessels was 3-4 times higher
 797 than that of blood vessels at all ages, n > 32. (C) IVCM image indicating the presence of lymph
 798 vessel (black arrow) and blood vessel (white arrow) at the same stromal depth. (D)
 799 Immunostaining of cornea sections revealed LYVE1-positive vessels (orange) and F4/80
 800 (green) cells throughout the stroma confirming the coincidence of macrophage infiltration and
 801 lymphangiogenesis in Het but not in Wt mouse corneas. Scale bars = 50μm.
 802



803
 804 **Figure 7.** β-III Tubulin immunostaining of corneal nerves in whole mount corneas. (Top row)
 805 Stromal nerve network, with central stromal nerves being scarce in Wt mice and highly
 806 prevalent in Het mice. (Bottom row) Vortex pattern of subbasal nerves in Wt mice and
 807 disrupted pattern of subbasal nerves in Het mice with anterior stromal nerves invading the
 808 subbasal layer. Scale bars = 500 μm.

809
 810
 811
 812



813
814
815
816
817

Figure 8. Immunolocalization of PAX6, Δ Np63, GPHA2, and KRT12 in the center, limbus, and central attachment zone in cross sections of corneas from Wt and Het mice with Grade 1 and 2 AAK. (First column) PAX6. (Second column) Δ Np63. (Third column) GPHA2. (Fourth column) KRT12. Nuclei are counterstained with DAPI (blue) in most sections.